American Journal of Computational Mathematics, 2026, 16(3), 168-193
https://www.scirp.org/journal/ajcm
ISSN Online: 2161-1211
ISSN Print: 2161-1203

A Computational Comparison of Q4 and Q8 Interpolation for Curvature-Preserving Surface Reconstruction

Kuldeep S. Rawat

Department of Mathematics, Computer Science, and Engineering Technology, Elizabeth City State University, Elizabeth City, USA
Email: ksrawat@ecsu.edu

How to cite this paper: Rawat, K.S. (2026) A Computational Comparison of Q4 and Q8 Interpolation for Curvature-Preserving Surface Reconstruction. *American Journal of Computational Mathematics*, **16**, 168-193.
https://doi.org/10.4236/ajcm.2026.163010

Received: June 11, 2026
Accepted: July 26, 2026
Published: July 29, 2026

Abstract

The four-node quadrilateral element (Q4) and the eight-node serendipity quadrilateral element (Q8) are standard interpolation models in numerical approximation and finite element analysis. This paper compares Q4 and Q8 interpolation for curvature-preserving surface reconstruction using a Hessian Frobenius-norm proxy and a Monge-patch formulation of surface normals. Interpolation error bounds derived from the Bramble-Hilbert lemma establish that Q8 achieves one higher order of Sobolev convergence than Q4 at every norm level: $O(h^3)$ versus $O(h^2)$ in L^2, $O(h^2)$ versus $O(h)$ in H^1, and $O(h)$ versus $O(h^0)$ in H^2, with the H^2 gap directly governing curvature fidelity. These theoretical rates are not directly measured by the single-element tests on analytic surfaces, which confirm polynomial reproduction and approximation behavior consistent with the predicted Q8 advantage; a mesh-refinement study on assembled elements is needed to verify the convergence orders computationally. Single-element experiments confirm exact polynomial reproduction for dome and saddle surfaces and show that, for a transcendental ripple surface, Q8 reduces height RMSE from 0.3310 to 0.0843 and normal-angle error from 37.47° to 15.02°. The results support a practical selection rule: Q4 is appropriate for height-only interpolation on locally planar or bilinear patches, while Q8 is preferred whenever surface normals or curvature are important.

Keywords

Q4 Interpolation, Q8 Serendipity Finite Element, Bramble-Hilbert Lemma, Curvature Preservation, Sobolev Norms, Surface Reconstruction

1. Introduction

Reconstructing a continuous surface from sparse measurements is a fundamental problem in computational mathematics, numerical modeling, computer vision, medical imaging, and scientific visualization [1] [2]. In a depth map, valid depth values may be missing due to occlusion, specular reflections, transparency, weak texture, range limitations, or sensor noise [3]. In structured-light and three-dimensional scanning, sparse or incomplete surface samples must be converted into a dense geometric representation [3] [4]. In biomedical imaging, organ surfaces may need to be reconstructed from sparse contours, segmented slices, or landmark samples [5]. In tissue deformation analysis, sparse tracked displacements must be converted into dense deformation fields.

Interpolation is one of the most direct methods for addressing such problems. Given nodal values at selected locations, an interpolant estimates the missing values between them. The choice of interpolation model, however, is not a neutral implementation detail. It encodes specific polynomial assumptions about the local geometry of the surface, and those assumptions determine both what can be represented exactly and how quickly the approximation error decreases as the element size is refined. A low-order interpolant may pass through the known data points but still reconstruct the wrong geometric structure between them. This distinction is critical when curvature, surface normals, or local shape carry physical meaning.

The four-node quadrilateral element, or Q4 element, is a standard bilinear interpolation model with polynomial degree of completeness equal to one [1] [2]. Its approximation space is

$$\mathcal{P}_{\mathrm{Q4}} = \mathrm{span}\{1, \xi, \eta, \xi\eta\} \tag{1}$$

which contains all polynomials of total degree at most one, plus the single mixed term $\xi\eta$. Because the pure quadratic monomials ξ^2 and η^2 are absent, Q4 cannot represent surfaces with quadratic curvature in either coordinate direction. This is not merely a quantitative limitation but a categorical one: no choice of nodal data can cause the Q4 interpolant to reproduce a dome or a parabolic edge profile exactly. The eight-node serendipity quadrilateral element, or Q8 element, extends Q4 by adding four edge-midpoint nodes [1]. Its polynomial space is complete to degree two:

$$\mathcal{P}_{\mathrm{Q8}} = \mathrm{span}\{1, \xi, \eta, \xi\eta, \xi^2, \eta^2, \xi^2\eta, \xi\eta^2\}, \tag{2}$$

which contains all monomials of total degree at most two, plus the two cubic serendipity terms $\xi^2\eta$ and $\xi\eta^2$. The inclusion of ξ^2 and η^2 gives Q8 the capacity to represent and exactly reproduce any surface that lies within this span.

The practical question motivating this paper is not whether Q8 is more accurate than Q4, as expected given the richer polynomial space. But: *When is Q8 worth the additional nodal and computational cost*?

The contribution of this paper is fourfold. First, it establishes the theoretical basis for the Q4 and Q8 comparison through polynomial completeness analysis, a formal polynomial reproduction theorem, Sobolev-norm interpolation error bounds derived from the Bramble-Hilbert lemma, and a convergence rate table. Second, it grounds the geometric metrics in the differential geometry of the Monge patch parameterization. Third, it provides a controlled computational illustration of polynomial reproduction and single-element approximation behavior consistent with these theoretical predictions. Fourth, it develops practical selection criteria that translate the mathematical findings into engineering guidance for curvature-sensitive surface reconstruction.

2. Q4 and Q8 Interpolation Models

Let $(\xi,\eta)\in\Omega=[-1,1]^2$ denote the coordinates of the normalized master element. A scalar surface height field is denoted by $z(\xi,\eta)$. The notation $H^s(\Omega)$ refers to the standard Sobolev space of functions with square-integrable weak derivatives up to order s, equipped with the norm $\|\cdot\|_{H^s(\Omega)}$ and seminorm $|\cdot|_{H^s(\Omega)}$.

2.1. Polynomial Completeness and the Monomial Structure

Table 1 lists all monomials up to total degree three, indicating their membership in $\mathcal{P}_{\mathrm{Q4}}$ and $\mathcal{P}_{\mathrm{Q8}}$, and identifies the degree of completeness of each space.

Table 1. Monomial content of Q4 and Q8 approximation spaces.

Monomial	Total Degree	In $\mathcal{P}_{\mathrm{Q4}}$	In $\mathcal{P}_{\mathrm{Q8}}$
1	0	Yes	Yes
ξ	1	Yes	Yes
η	1	Yes	Yes
ξ^2	2	**No**	Yes
$\xi\eta$	2	Yes	Yes
η^2	2	**No**	Yes
ξ^3	3	No	No
$\xi^2\eta$	3	No	Yes
$\xi\eta^2$	3	No	Yes
η^3	3	No	No
Degree of completeness		**1**	**2**
Dimension		**4**	**8**

The degree of completeness is the largest integer p such that every monomial of total degree $\le p$ belongs to the space; Q4 achieves $p = 1$ (missing ξ^2 and η^2) while Q8 achieves $p = 2$. This distinction governs approximation order, as made precise in Section 2.6 [1] [6] [7]. **Figure 1** illustrates the node configurations for both elements on the master element.

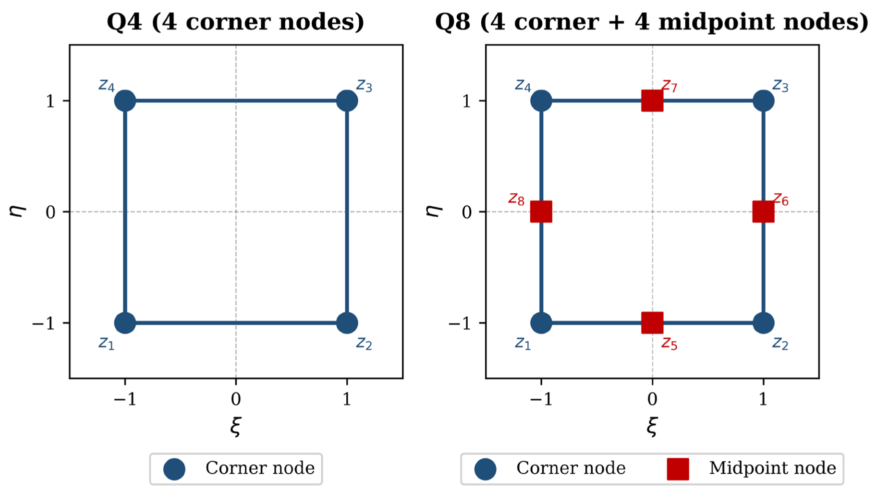

Figure 1. Q4 and Q8 Node Layout. Node configurations for Q4 and Q8 interpolation elements on the normalized master element $[-1, 1]^2$. Q4 uses four corner nodes; Q8 augments these with four edge-midpoint nodes.

Figure 1 establishes the geometric foundation for the entire comparison. The left panel shows the Q4 element, which samples the surface only at its four corners: (−1, −1), (1, −1), (1, 1), and (−1, 1). Because each edge of the Q4 element is controlled by exactly two endpoint values, the interpolated profile along any edge is constrained to be a straight line. This means that any curvature present in the true surface between two corners is invisible to Q4—it has no nodal information from which to detect or reconstruct bending.

The right panel shows the Q8 element, which retains all four corner nodes and adds one midpoint node on each of the four edges: (0, −1), (1, 0), (0, 1), and (−1, 0). This seemingly modest addition has a profound effect. Each edge is now controlled by three values, *i.e.*, two endpoints and one midpoint, which is the minimum information needed to fit a parabola. As a result, Q8 can sense and exactly reproduce quadratic edge curvature, and can approximate more general smooth edge curvature more accurately than Q4. The figure makes it visually clear that the difference between Q4 and Q8 is not a global modeling choice but a local sampling one: Q8 simply captures more geometric information per element by reading the surface at its edge midpoints.

2.2. Q4 Bilinear Interpolation

The four Q4 nodes are placed at the element corners:

$$(\xi_1,\eta_1)=(-1,-1),(\xi_2,\eta_2)=(1,-1),(\xi_3,\eta_3)=(1,1),(\xi_4,\eta_4)=(-1,1) \tag{3}$$

Given nodal values $z_k = z(\xi_k,\eta_k)$ for $k = 1,2,3,4$, the Q4 interpolant is

$$z_{Q4}(\xi,\eta)=\sum_{k=1}^{4} N_k(\xi,\eta)\, z_k \tag{4}$$

where the bilinear shape functions are

$$N_1 = \frac{1}{4}(1-\xi)(1-\eta) \tag{5a}$$

$$N_2 = \frac{1}{4}(1+\xi)(1-\eta) \tag{5b}$$

$$N_3 = \frac{1}{4}(1+\xi)(1+\eta) \tag{5c}$$

$$N_4 = \frac{1}{4}(1-\xi)(1+\eta) \tag{5d}$$

These functions satisfy two fundamental properties, the Kronecker delta and the partition of unity. The Kronecker-delta property states

$$N_k\left(\xi_j, \eta_j\right) = \delta_{kj},\ j,k \in \{1,2,3,4\}, \tag{6}$$

ensuring that the interpolant passes through the nodal values exactly. The partition of unity property states

$$\textstyle\sum_{k=1}^{4} N_k(\xi,\eta) = 1\ \ \forall(\xi,\eta) \in \Omega, \tag{7}$$

which guarantees that constant fields are reproduced exactly and is a necessary condition for consistency [1] [2].

2.3. Q8 Serendipity Interpolation

The Q8 element uses the four corner nodes of Q4 plus four edge-midpoint nodes:

$$(\xi_5,\eta_5) = (0,-1), (\xi_6,\eta_6) = (1,0), (\xi_7,\eta_7) = (0,1), (\xi_8,\eta_8) = (-1,0) \tag{8}$$

Given nodal values $z_k = z(\xi_k, \eta_k)$ for $k = 1,\cdots,8$, the Q8 interpolant is

$$z_{Q8}(\xi,\eta) = \sum_{k=1}^{8} \phi_k(\xi,\eta) z_k \tag{9}$$

The serendipity shape functions for corner nodes are

$$\phi_1 = \frac{1}{4}(1-\xi)(1-\eta)(-\xi-\eta-1) \tag{10a}$$

$$\phi_2 = \frac{1}{4}(1+\xi)(1-\eta)(\xi-\eta-1) \tag{10b}$$

$$\phi_3 = \frac{1}{4}(1+\xi)(1+\eta)(\xi+\eta-1) \tag{10c}$$

$$\phi_4 = \frac{1}{4}(1-\xi)(1+\eta)(-\xi+\eta-1) \tag{10d}$$

and for edge-midpoint nodes are

$$\phi_5 = \frac{1}{2}(1-\xi^2)(1-\eta) \tag{11a}$$

$$\phi_6 = \frac{1}{2}(1+\xi)(1-\eta^2) \tag{11b}$$

$$\phi_7 = \frac{1}{2}(1-\xi^2)(1+\eta) \tag{11c}$$

$$\phi_8 = \frac{1}{2}(1-\xi)(1-\eta^2) \tag{11d}$$

The Q8 shape functions satisfy the same Kronecker-delta and partition of unity properties [1] [2]. Their polynomial span is $\mathcal{P}_{Q8}$, which is complete to degree two [1] [2] [8].

2.4. Why the Comparison Is Not Trivial

It is mathematically expected that Q8 can outperform Q4 on curved surfaces because Q8 has more nodal information and a richer approximation space [9]. Therefore, the purpose of this paper is to quantify the geometric consequence of the added Q8 degrees of freedom. The comparison asks whether the extra nodal information preserves quantities that matter in surface reconstruction: height, curvature, and surface orientation. This distinction is important for computational decision-making. In many applications, Q4 may be sufficient. If the surface is nearly planar over the element, or if only corner samples are available, Q4 is efficient and appropriate. If the surface is locally smooth but curved, and if midpoint samples are available or can be estimated reliably, Q8 may be justified because it preserves curvature and normals more accurately. Modifications to the standard Q8 element have also been studied [10].

The closed-form shape functions used here may be viewed as the inverse of a fixed nodal collocation system on the reference element. Since the nodes are fixed and the nodal functionals are unisolvent on the stated polynomial spaces, the reference interpolation operators are bounded. Under affine scaling to shape-regular physical elements, these constants remain independent of the element size h.

2.5. Polynomial Reproduction Theorem

The fundamental exactness property of both interpolants is stated as follows.

Theorem 1 (Polynomial reproduction of Q4 and Q8). Let $\Omega = [-1,1]^2$ be the reference square and let $\mathcal{P}_{Q4}$ and $\mathcal{P}_{Q8}$ denote the polynomial spaces defined in Equation (1) and Equation (2), respectively.

(i) The Q4 interpolation operator $\mathcal{I}_{Q4}$ reproduces every polynomial in $\mathcal{P}_{Q4}$.

(ii) The Q8 interpolation operator $\mathcal{I}_{Q8}$ reproduces every polynomial in $\mathcal{P}_{Q8}$.

(iii) There exist polynomials $f \in \mathcal{P}_{Q8} \setminus \mathcal{P}_{Q4}$ that are not reproduced by $\mathcal{I}_{Q4}$.

Proof. Consider first the Q4 element. The reference nodes $\{(\xi_k, \eta_k)\}_{k=1}^{4}$ are the four corners of Ω, and the Q4 shape functions $\{N_k\}_{k=1}^{4}$ defined in Equation (5a-5d) are Lagrange shape functions satisfying the Kronecker delta property

$$N_k(\xi_j, \eta_j) = \delta_{kj}, 1 \le j, k \le 4, \tag{12}$$

and the partition of unity $\sum_{k=1}^{4} N_k \equiv 1$. The corresponding nodal evaluation functionals $\ell_k : C^0(\Omega) \to \mathbb{R}$, $\ell_k(f) = f(\xi_k, \eta_k)$, are linearly independent on the four–dimensional space $\mathcal{P}_{Q4}$; hence they form a unisolvent set of degrees of freedom for $\mathcal{P}_{Q4}$. Equivalently, the only polynomial $p \in \mathcal{P}_{Q4}$ satisfying $\ell_k(p) = 0$ for all k is the zero polynomial.

By definition, the Q4 interpolation operator $\mathcal{I}_{Q4} : C^0(\Omega) \to \mathcal{P}_{Q4}$ is given by

$$\mathcal{I}_{Q4} f(\xi,\eta) = \sum_{k=1}^{4} f(\xi_k,\eta_k) N_k(\xi,\eta), \tag{13}$$

so that $\ell_k(\mathcal{I}_{Q4} f) = f(\xi_k,\eta_k)$ for all k. Now let $f \in \mathcal{P}_{Q4}$. Then both f and $\mathcal{I}_{Q4} f$ belong to $\mathcal{P}_{Q4}$ and satisfy

$$\ell_k(f) = \ell_k(\mathcal{I}_{Q4} f), k = 1,2,3,4. \tag{14}$$

By unisolvency, $f = \mathcal{I}_{Q4} f$ on Ω, which proves (i).

The proof of (ii) is analogous for Q8. The eight serendipity shape functions $\{\phi_k\}_{k=1}^{8}$ defined in Equation (10) and Equation (11) satisfy

$$\phi_k(\xi_j,\eta_j) = \delta_{kj}, 1 \le j,k \le 8, \tag{15}$$

at the eight Q8 nodes, and $\sum_{k=1}^{8} \phi_k \equiv 1$. The nodal evaluation functionals $\ell_k(f) = f(\xi_k,\eta_k)$ are unisolvent for the eight–dimensional polynomial space $\mathcal{P}_{Q8}$. The Q8 interpolation operator

$$\mathcal{I}_{Q8} f(\xi,\eta) = \sum_{k=1}^{8} f(\xi_k,\eta_k) \phi_k(\xi,\eta) \tag{16}$$

therefore satisfies $\mathcal{I}_{Q8} f = f$ for every $f \in \mathcal{P}_{Q8}$, establishing (ii).

For (iii), consider the dome

$$f(\xi,\eta) = 1 - \frac{\xi^2 + \eta^2}{2}, \tag{17}$$

which lies in $\mathcal{P}_{Q8}$ but not in $\mathcal{P}_{Q4}$ because it contains the pure quadratic monomials ξ^2 and η^2 absent from $\mathcal{P}_{Q4}$. At each Q4 corner node $\pm1, \pm1$ we have

$$f(\pm1,\pm1) = 1 - \frac{1+1}{2} = 0, \tag{18}$$

so $\mathcal{I}_{Q4} f$ is the unique polynomial in $\mathcal{P}_{Q4}$ that vanishes at all four corners. Any bilinear polynomial with four zero corner values is identically zero on Ω, hence $\mathcal{I}_{Q4} f \equiv 0$. Since $f(0,0) = 1$, it follows that $\mathcal{I}_{Q4} f \ne f$, and in particular $\| f - \mathcal{I}_{Q4} f \|_{L^\infty(\Omega)} \ge 1$. This shows that Q4 does not reproduce all functions in $\mathcal{P}_{Q8}$, completing the proof. □

Remark 1. Since $\mathcal{I}_{Q4} f \in \mathcal{P}_{Q4}$, Q4 cannot reproduce any function $f \notin \mathcal{P}_{Q4}$ exactly over the element. However, for some functions outside the Q4 span, the resulting error may be small or acceptable for a given application.

2.6. Consistency, Patch Test, and Stability

Consistency. Both Q4 and Q8 satisfy the consistency condition for interpolation on the reference element: they exactly reproduce all constant and linear fields. This is guaranteed by the partition of unity and Kronecker-delta properties of the shape functions. In the interpolation setting considered here, the relevant analog of the finite element patch test is the exact reproduction of constant and linear fields, which both elements satisfy [1] [6].

Stability. The closed-form shape functions for Q4 and Q8 may be viewed as the inverses of fixed nodal collocation systems on the reference element. For Q4, the four shape functions are the unique bilinear basis dual to the four corner nodal functionals. For Q8, the eight shape functions are the unique serendipity basis dual to the eight nodal functionals (four corners and four edge midpoints). In both cases, the nodal functionals are unisolvent on their respective polynomial spaces, meaning the only function in the space that vanishes at all nodes is the zero function [7] [8]. This unisolvence guarantees that the interpolation operators $\mathcal{I}_{\mathrm{Q4}}$ and $\mathcal{I}_{\mathrm{Q8}}$ are well-defined and bounded on the reference element. Under affine scaling to shape-regular physical elements, the operator norms remain bounded independently of the element size h [7] [11].

Remark 2. No Vandermonde system is solved during interpolation at runtime. The shape functions are precomputed in closed form, and interpolation at any point (ξ,η) requires only the evaluation of eight scalar functions and a weighted sum. The stability statement above refers to the conditioning of the underlying nodal collocation map, not to an iterative or linear-system computation.

2.7. Interpolation Error Bounds

Theorem 2 (Elementwise interpolation error for Q4 and Q8). Let $\{K_h\}$ be a family of shape-regular quadrilateral elements obtained by affine images of the reference square $\Omega=[-1,1]^2$, with element diameter $h=\mathrm{diam}(K_h)$. Let $\mathcal{I}_h$ denote either the Q4 or Q8 nodal interpolation operator, defined by Equation (4) or Equation (9) on Ω and extended to K_h by composition with the reference mapping.

Assume $f\in H^{p+1}(K_h)$, where p is the polynomial reproduction degree of the interpolant ($p=1$ for Q4, $p=2$ for Q8; see **Table 1**).

Then there exists a constant $C>0$, independent of h and f, such that for $j=0,1,2$ the following bound holds:

$$\left\| f-\mathcal{I}_h f \right\|_{H^j(K_h)} \le C\,h^{p+1-j}\,\left| f \right|_{H^{p+1}(K_h)}. \tag{19}$$

Proof. On the reference element Ω, the Q4 and Q8 interpolation operators $\mathcal{I}_{\mathrm{Q4}}$ and $\mathcal{I}_{\mathrm{Q8}}$ are linear projectors onto $\mathcal{P}_{\mathrm{Q4}}$ and $\mathcal{P}_{\mathrm{Q8}}$, respectively. By Theorem 1 and the degree-of-completeness summary in **Table 1**, $\mathcal{I}_{\mathrm{Q4}}$ reproduces all polynomials of degree at most $p=1$, and $\mathcal{I}_{\mathrm{Q8}}$ reproduces all polynomials of degree at most $p=2$.

Each $\mathcal{I}_h$ is defined elementwise by pullback from Ω: if $F_h:\Omega\to K_h$ is the affine map, then $\mathcal{I}_h f=\left(\mathcal{I}_{ref}\left(f\circ F_h\right)\right)\circ F_h^{-1}$, where $\mathcal{I}_{ref}$ is $\mathcal{I}_{\mathrm{Q4}}$ or $\mathcal{I}_{\mathrm{Q8}}$ on Ω. The shape-regularity of $\{K_h\}$ implies that the Jacobians of F_h and F_h^{-1} are uniformly bounded in h, and the norms $\|\cdot\|_{H^m(K_h)}$ and $\|\cdot\|_{H^m(\Omega)}$ are equivalent up to constants depending only on the shape-regularity and on m.

On Ω, the operators $\mathcal{I}_{\mathrm{Q4}}$ and $\mathcal{I}_{\mathrm{Q8}}$ are bounded linear maps on $H^{p+1}(\Omega)$, with operator norms independent of h. They reproduce all polynomials of degree at most p. Therefore, the hypotheses of the Bramble–Hilbert lemma are satisfied on each element K_h: there exists a polynomial $q\in\mathbb{P}_p(K_h)$ such that

$$\left\| f - q \right\|_{H^j(K_h)} \le C_1 h^{p+1-j} \left| f \right|_{H^{p+1}(K_h)}, j = 0,1,2, \tag{20}$$

with C_1 independent of h and f.

Since $\mathcal{I}_h$ reproduces all polynomials of degree at most p, we have $\mathcal{I}_h q = q$. Thus,

$$f - \mathcal{I}_h f = (f - q) - \mathcal{I}_h (f - q). \tag{21}$$

Taking the $H^j(K_h)$ norm and using the linearity and boundedness of $\mathcal{I}_h$ on $H^{p+1}(K_h)$, there exists $C_2 > 0$, independent of h and f, such that

$$\left\| f - \mathcal{I}_h f \right\|_{H^j(K_h)} \le \left\| f - q \right\|_{H^j(K_h)} + \left\| \mathcal{I}_h (f - q) \right\|_{H^j(K_h)} \le (1 + C_2) \left\| f - q \right\|_{H^j(K_h)}. \tag{22}$$

Combining this with the Bramble–Hilbert estimate above yields

$$\left\| f - \mathcal{I}_h f \right\|_{H^j(K_h)} \le C h^{p+1-j} \left| f \right|_{H^{p+1}(K_h)}, \tag{23}$$

where $C = (1 + C_2) C_1$ depends only on the element shape-regularity and the interpolation operator, but not on h or f. This proves Equation (19). □

Corollary 1 (Error orders for Q4 and Q8). For Q4, $p = 1$, so Equation (19) gives

$$\left\| f - \mathcal{I}_{\mathrm{Q4}} f \right\|_{L^2(K_h)} = \mathcal{O}(h^2), \left\| f - \mathcal{I}_{\mathrm{Q4}} f \right\|_{H^1(K_h)} = \mathcal{O}(h), \left\| f - \mathcal{I}_{\mathrm{Q4}} f \right\|_{H^2(K_h)} = \mathcal{O}(h^0), \tag{24}$$

whereas for Q8, $p = 2$, one obtains

$$\left\| f - \mathcal{I}_{\mathrm{Q8}} f \right\|_{L^2(K_h)} = \mathcal{O}(h^3), \left\| f - \mathcal{I}_{\mathrm{Q8}} f \right\|_{H^1(K_h)} = \mathcal{O}(h^2), \left\| f - \mathcal{I}_{\mathrm{Q8}} f \right\|_{H^2(K_h)} = \mathcal{O}(h). \tag{25}$$

These convergence orders are summarized in Table 2 and, in particular, show that Q8 achieves one higher order of convergence than Q4 in each Sobolev norm level $j = 0,1,2$.

Table 2. Theoretical convergence orders for Q4 and Q8 in Sobolev norms.

Norm	Q4 Order (p = 1)	Q8 Order (p = 2)	Geometric Quantity
$L^2(\Omega)$	$\mathcal{O}(h^2)$	$\mathcal{O}(h^3)$	Height-field (L^2 norm)
$H^1(\Omega)$	$\mathcal{O}(h^1)$	$\mathcal{O}(h^2)$	Surface slopes and normals
$H^2(\Omega)$	$\mathcal{O}(h^0)^\dagger$	$\mathcal{O}(h^1)$	Curvature (Hessian-based proxy)

†The $\mathcal{O}(h^0)$ bound means the error estimate does not decrease with h; it does not imply the error grows or diverges.

Remark 3 (Scope of the numerical experiments). The single-element experiments in Section 6 confirm polynomial reproduction and single-element approximation behavior on the fixed master element with $h = 2$. They do not directly demonstrate asymptotic convergence orders, which are statements about a family of elements with $h \to 0$ and would require a mesh-refinement study. The error ratios observed in Table 3 are consistent with the qualitative advantage predicted by the bounds in Theorem 2 and Table 2, but they should not be interpreted as empirical measurements of convergence rates. A mesh-refinement study is therefore identified as a direction for future work in Section 9.

3. Curvature-Preservation Metrics and Differential Geometry

This section introduces the geometric tools used to measure curvature preservation, relating the Monge-patch parameterization to surface normals, the fundamental forms, and a Hessian-based curvature proxy aligned with the H^2 error analysis.

3.1. The Monge Patch Parameterization

A height field $z = f(\xi,\eta)$ over the master element defines a surface patch through the Monge (graph) parameterization [12]:

$$\mathrm{r}(\xi,\eta) = \left(\xi,\eta, f(\xi,\eta)\right)^{\top}. \tag{26}$$

The two tangent vectors are

$$\mathrm{r}_{\xi} = \left(1,0, f_{\xi}\right)^{\top}, \mathrm{r}_{\eta} = \left(0,1, f_{\eta}\right)^{\top}. \tag{27}$$

The upward-pointing surface normal is obtained as their cross product:

$$\mathrm{n} = \mathrm{r}_{\xi} \times \mathrm{r}_{\eta} = \left(-f_{\xi}, -f_{\eta}, 1\right)^{\top}. \tag{28}$$

This derivation shows that the formula $\mathrm{n} = \left[-f_{\xi}, -f_{\eta}, 1\right]^{\top}$ is not an arbitrary choice but the upward-pointing normal direction to the Monge patch, obtained by convention. The unit normal is

$$\hat{\mathrm{n}} = \frac{\left(-f_{\xi}, -f_{\eta}, 1\right)^{\top}}{\sqrt{f_{\xi}^2 + f_{\eta}^2 + 1}}. \tag{29}$$

The first fundamental form of the Monge patch has coefficients

$$E = 1 + f_{\xi}^2, F = f_{\xi} f_{\eta}, G = 1 + f_{\eta}^2, \tag{30}$$

and the second fundamental form has coefficients

$$L = \frac{f_{\xi\xi}}{\sqrt{f_{\xi}^2 + f_{\eta}^2 + 1}}, M = \frac{f_{\xi\eta}}{\sqrt{f_{\xi}^2 + f_{\eta}^2 + 1}}, N = \frac{f_{\eta\eta}}{\sqrt{f_{\xi}^2 + f_{\eta}^2 + 1}}. \tag{31}$$

3.2. Hessian-Based Curvature Proxy

The Hessian of the height field $z = f(\xi,\eta)$ is the symmetric matrix

$$H_f = \begin{pmatrix} f_{\xi\xi} & f_{\xi\eta} \\ f_{\xi\eta} & f_{\eta\eta} \end{pmatrix}. \tag{32}$$

The Hessian-based curvature proxy is the Frobenius norm of H_f:

$$\kappa_H = \left\| H_f \right\|_F = \sqrt{f_{\xi\xi}^2 + 2 f_{\xi\eta}^2 + f_{\eta\eta}^2}. \tag{33}$$

In the small-slope regime where $f_{\xi}^2 + f_{\eta}^2 \ll 1$, the shape operator simplifies to $S \approx H_f$ and the following relations hold:

$$H_{\text{mean}} = \frac{1}{2}(\kappa_1 + \kappa_2) = \frac{1}{2}\Delta f, \tag{34a}$$

$$K = \kappa_1\kappa_2 = \det(H_f) = f_{\xi\xi} f_{\eta\eta} - f_{\xi\eta}^2, \tag{34b}$$

$$\kappa_H^2 = \kappa_1^2 + \kappa_2^2 = 4H_{\text{mean}}^2 - 2K. \tag{34c}$$

These relations hold in the small-slope approximation. For surfaces with larger gradients, κ_H remains a well-defined and interpolation-sensitive second-derivative measure, but it should be interpreted as a height-field curvature proxy rather than the exact principal curvature magnitude of the Monge surface.

The proxy κ_H is preferred over the Laplacian $\Delta f = f_{\xi\xi} + f_{\eta\eta}$ for the following reason. Consider the saddle $z = \xi^2/2 - \eta^2/2$, which has $f_{\xi\xi} = 1$ and $f_{\eta\eta} = -1$. Then $\Delta f = 0$ identically, incorrectly suggesting zero curvature, while

$$\kappa_H = \sqrt{1^2 + 2\cdot 0^2 + (-1)^2} = \sqrt{2} \neq 0, \tag{35}$$

correctly indicating strong bending. The curvature proxy error metric is therefore

$$E_\kappa(\xi,\eta) = \left|\kappa_{H,\text{true}}(\xi,\eta) - \kappa_{H,\text{interp}}(\xi,\eta)\right|. \tag{36}$$

The principal curvatures κ_1 and κ_2 are the eigenvalues of the shape operator $S = I^{-1}II$, where I and II are the matrices of the first and second fundamental forms. For the dome surface $z = 1 - (\xi^2 + \eta^2)/2$, the Hessian eigenvalues of the height field are $-1, -1$, giving a constant Hessian-based curvature proxy $\kappa_H = \sqrt{2}$. In the small-slope regime, the Hessian eigenvalues approximate the principal curvatures, but the exact principal curvatures of the Monge surface vary with (ξ,η) because the first fundamental form depends on the gradient.

3.3. Height Error

The pointwise height error is

$$E_z(\xi,\eta) = \left|z_{\text{true}}(\xi,\eta) - z_{\text{interp}}(\xi,\eta)\right|. \tag{37}$$

The height RMSE over the discrete grid Ω_h of 201 × 201 points is

$$\|E_z\|_{\text{RMS}} = \sqrt{\frac{1}{|\Omega_h|}\sum_{i,j} E_z(\xi_i,\eta_j)^2}, \tag{38}$$

providing a discrete approximation to the $L^2(\Omega)$ norm of the interpolation error and directly connecting the numerical measure to the theoretical L^2 bound of Theorem 2.

3.4. Normal-Angle Error

Using the Monge patch formulation of Section 3.1, the unit normal to the reconstructed surface is

$$\hat{n}_{\text{interp}} = \frac{\left(-(z_{\text{interp}})_\xi, -(z_{\text{interp}})_\eta, 1\right)^\top}{\left\|\left(-(z_{\text{interp}})_\xi, -(z_{\text{interp}})_\eta, 1\right)\right\|_2}, \tag{39}$$

and the normal-angle error at each grid point is

$$E_n(\xi,\eta) = \arccos\left(\hat{\mathrm{n}}_{\mathrm{true}}\hat{\mathrm{n}}_{\mathrm{interp}}\right), \tag{40}$$

reported in degrees. Since n depends on the first derivatives of z, the normal-angle error is governed by the H^1 interpolation error. By Theorem 2, Q8 provides $\mathcal{O}(h^2)$ convergence in H^1 versus $O(h)$ for Q4, predicting systematically smaller normal-angle errors for Q8, as confirmed in **Table 3**.

4. Numerical Test Surfaces

Three test surfaces, dome, saddle, and transcendental ripple, were used on the master element $\Omega = [-1,1]^2$.

4.1. Dome Surface

$$z_{\mathrm{dome}}(\xi,\eta) = 1 - \frac{\xi^2+\eta^2}{2} \tag{41}$$

This surface belongs to $\mathcal{P}_{\mathrm{Q8}}$ but not to $\mathcal{P}_{\mathrm{Q4}}$. By Theorem 1 (ii), Q8 reproduces it exactly; by part (iii), Q4 does not. The Hessian is

$$\boldsymbol{H}_{f_{\mathrm{dome}}} = \begin{pmatrix} -1 & 0 \\ 0 & -1 \end{pmatrix} = -\boldsymbol{I}_2 \tag{42}$$

giving Hessian eigenvalues −1 and −1, a constant Hessian-based curvature proxy $\kappa_H = \sqrt{2}$, and a small-slope approximation to mean curvature of −1. The exact principal curvatures of the Monge surface vary with (ξ, η) because the first fundamental form depends on the gradient; the Hessian eigenvalues equal the principal curvatures only in the small-slope regime.

4.2. Saddle Surface

$$z_{\mathrm{saddle}}(\xi,\eta) = \xi\eta + \frac{\xi^2-\eta^2}{3} \tag{43}$$

This surface belongs to $\mathcal{P}_{\mathrm{Q8}} \setminus \mathcal{P}_{\mathrm{Q4}}$. The term $\xi\eta$ is in $\mathcal{P}_{\mathrm{Q4}}$; the terms $\xi^2/3$ and $-\eta^2/3$ are not. The Hessian is

$$\boldsymbol{H}_{f_{\mathrm{saddle}}} = \begin{pmatrix} 2/3 & 1 \\ 1 & -2/3 \end{pmatrix} \tag{44}$$

The small-slope approximation to Gaussian curvature (the Hessian determinant) is

$$K = \det\left(\boldsymbol{H}_{f_{\mathrm{saddle}}}\right) = \frac{2}{3}\cdot\left(-\frac{2}{3}\right) - 1^2 = -\frac{4}{9} - 1 = -\frac{13}{9} < 0 \tag{45}$$

confirming the saddle character. (The exact Gaussian curvature of the Monge surface includes a denominator of $\left(1+f_\xi^2+f_\eta^2\right)^2$ and is not identically equal to $\det\left(H_f\right)$.) The Hessian curvature magnitude is

$$\kappa_H = \sqrt{\left(\frac{2}{3}\right)^2 + 2\cdot 1^2 + \left(-\frac{2}{3}\right)^2} = \sqrt{\frac{8}{9}+2} = \frac{\sqrt{26}}{3} \approx 1.700 \tag{46}$$

4.3. Transcendental Ripple Surface

$$z_{\text{ripple}}(\xi,\eta)=\frac{1}{2}\sin(2\xi)\cos(2\eta) \tag{47}$$

This surface is outside both Q4 and Q8 polynomial spaces. Its Taylor expansion near $(0,0)$ begins

$$z_{\text{ripple}}=\xi-2\xi\eta^2-\frac{2}{3}\xi^3+\cdots, \tag{48}$$

which contains cubic and higher terms not present in either $\mathcal{P}_{Q4}$ or $\mathcal{P}_{Q8}$. The ripple is included to test approximation behavior rather than exact polynomial reproduction. This is important because real surfaces in depth imaging, scanning, and biomedical reconstruction are rarely exact low-order polynomials.

The Hessian is

$$\boldsymbol{H}_{f_{\text{ripple}}}=\begin{pmatrix}-2\sin(2\xi)\cos(2\eta) & -2\cos(2\xi)\sin(2\eta)\\ -2\cos(2\xi)\sin(2\eta) & -2\sin(2\xi)\cos(2\eta)\end{pmatrix} \tag{49}$$

which varies strongly over Ω, making curvature preservation a non-trivial challenge for a single-element interpolant.

5. Computational Implementation

All computations were performed in Python using NumPy, Pandas, and Matplotlib. The master element was discretized on a 201 × 201 uniform grid, giving grid spacings $\Delta\xi=\Delta\eta=0.01$. Nodal values were sampled exactly at the Q4 and Q8 node locations from the analytic surface definitions. No measurement noise, smoothing, optimization, regularization, or training was applied. This design isolates the approximation behavior of each interpolation space. For the polynomial dome and saddle cases, centered finite differences recover the exact second derivatives up to floating-point roundoff; the residual Q8 curvature MAE of order 10^{-13} therefore reflects roundoff and numerical differentiation residual rather than interpolation error. Specifically, first-order partial derivatives (used for the surface normal at each grid point) were approximated by second-order centered differences, $\left(f_{i+1,j}-f_{i-1,j}\right)/(2\Delta\xi)$, and second-order partial derivatives (used for the Hessian entries) by $\left(f_{i+1,j}-2f_{i,j}+f_{i-1,j}\right)/\Delta\xi^2$, with analogous formulas in η and $\left(f_{i+1,j+1}-f_{i+1,j-1}-f_{i-1,j+1}+f_{i-1,j-1}\right)/(4\Delta\xi\Delta\eta)$ for the mixed partial; at the four grid boundaries, second-order one-sided differences were substituted. The height RMSE provides a discrete approximation to the $L^2(\Omega)$ norm bound of Theorem 2; the normal-angle error connects to the H^1 bound; and the curvature MAE connects to the H^2 bound. Together, these three metrics assess interpolation quality across the Sobolev norm hierarchy of Theorem 2.

6. Results

All numerical experiments in this section are performed on the normalized master element $\Omega=[-1,1]^2$, corresponding to a fixed element diameter $h=2$. For each test surface (dome, saddle, and ripple), we compare Q4 and Q8 reconstructions on this single element and evaluate height, normal, and curvature-proxy errors. Table 3 summarizes the resulting error metrics.

Table 3. Q4 and Q8 reconstruction errors on dome, saddle, and transcendental ripple surfaces.

Surface	Method	Height RMSE	Max Height Error	Curvature MAE	Mean Normal-Angle Error
Dome	Q4	6.9667×10^{-1}	1.0000	1.4142	36.17°
Dome	Q8	6.2096×10^{-17}	2.2204×10^{-16}	3.5383×10^{-13}	2.49×10^{-7}°
Saddle	Q4	1.4195×10^{-1}	3.3333×10^{-1}	2.8546×10^{-1}	20.97°
Saddle	Q8	6.7848×10^{-17}	4.4409×10^{-16}	2.9488×10^{-13}	2.19×10^{-7}°
Transcendental Ripple	Q4	3.3099×10^{-1}	6.5757×10^{-1}	1.8504	37.47°
Transcendental Ripple	Q8	8.4273×10^{-2}	1.9555×10^{-1}	9.8559×10^{-1}	15.02°

Table 3 reports four error metrics for each combination of surface and interpolation method, providing a comprehensive picture of reconstruction quality across height, curvature, and orientation dimensions. These metrics are consistent with the polynomial reproduction properties of Theorem 1, the interpolation error bounds of Theorem 2, and the Sobolev-order hierarchy in Table 2.

For the dome, the contrast between Q4 and Q8 is stark and unambiguous. Q4's height RMSE of 0.6967 and maximum height error of 1.0000 reflect a complete failure to reproduce the surface—these are not small approximation errors but fundamental misrepresentations. The curvature MAE of 1.4142 confirms that Q4 contributes no bending information. The normal-angle error of 36.17 degrees means that the reconstructed surface normals point in substantially wrong directions over most of the element—a severe problem for any application that uses normals for rendering, registration, or shape analysis. Q8's errors for the dome are all at machine precision (on the order of 10^{-13} to 10^{-17}), confirming exact polynomial reproduction.

For the saddle, Q4's errors are smaller than on the dome—height RMSE 0.14195, normal-angle error 20.97 degrees—because Q4 can represent the $\xi\eta$ bilinear component. However, a normal-angle error of nearly 21 degrees still represents a substantial geometric distortion. Q8 again achieves machine-precision accuracy across all metrics.

For the transcendental ripple, neither method is exact. Q4's errors are the largest in absolute terms for the height metric (RMSE 0.33099, max 0.6576) and the largest for the normal-angle metric (37.47 degrees). Q8 reduces height RMSE by 74.5% to 0.0843, reduces maximum height error to 0.19555, and halves the normal-angle error to 15.02 degrees. The curvature MAE drops from 1.8504 to 0.9856, a 46.7% reduction. These reductions are meaningful in practical terms: a 15-degree normal error is still non-trivial but is far more acceptable than a 37-degree error for most geometric processing tasks.

In summary, the table supports two distinct conclusions. First, when a surface lies in the Q8 polynomial span (dome, saddle), Q8 is not merely better than Q4—

it is exact, while Q4 fails categorically. Second, when a surface lies outside both polynomial spans (ripple), Q8 still provides substantially better approximation, demonstrating that its advantage is not limited to special cases.

6.1. Dome Results

Figure 2 shows the dome surface reconstruction comparison panels. The dome surface $z = 1 - (\xi^2 + \eta^2)/2$ is a smooth, symmetric, concave-down paraboloid. Its defining feature is pure quadratic curvature in both coordinate directions, with a peak at the origin and equal values of zero at all four corners. Because all four corners share the same height ($z = 0$), Q4 receives identical corner values and can extract no curvature information from them whatsoever. The Q4 bilinear polynomial, which spans only {1, ξ, η, $\xi\eta$}, is therefore forced to reconstruct a flat surface—the bilinear interpolant through four equal corner values is identically zero everywhere, giving a height RMSE of 0.6967 and a maximum height error of 1.0000 at the dome's peak. The Q4 reconstruction panel in the center confirms this: the dome's central bulge is entirely absent, replaced by a flat or nearly flat surface.

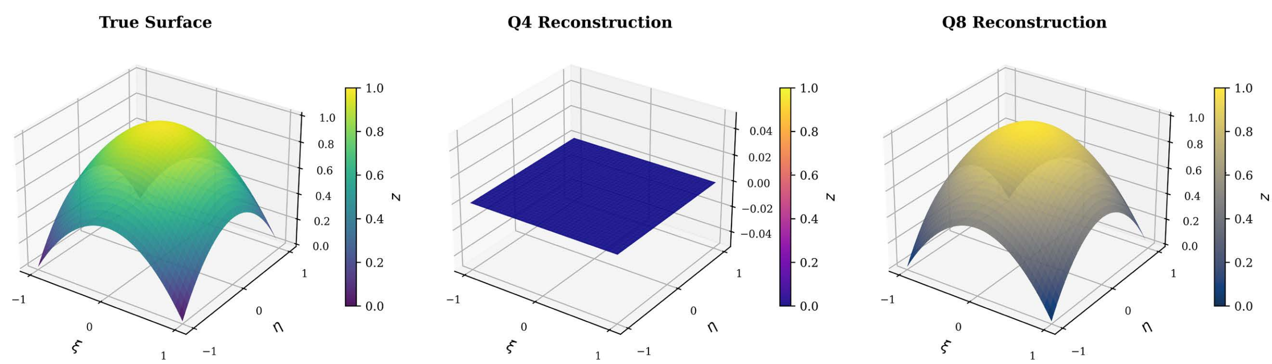

Figure 2. Dome surface comparison. True dome surface and Q4 and Q8 reconstructions. Q4 collapses the quadratic curvature to a near-flat bilinear surface; Q8 reproduces the dome to numerical precision.

The Q8 reconstruction panel on the right tells the opposite story. The midpoint nodes sample the dome at its edges, where z takes non-zero values that directly encode the parabolic profile. Q8's polynomial span includes ξ^2 and η^2, so it possesses exactly the terms needed to fit the dome. The result is exact reproduction to machine precision: a height RMSE of 6.21×10^{-17} and a normal-angle error of 2.49×10^{-7} degrees, both numerically zero. This figure is the clearest illustration in the paper of the categorical difference between the two interpolants: Q4 fails completely on a surface it cannot represent, while Q8 succeeds exactly.

6.2. Saddle Results

Figure 3 shows the saddle surface reconstruction comparison panels. The saddle surface $z = \xi\eta + (\xi^2 - \eta^2)/3$ is a more demanding and nuanced test than the dome, as it contains two structurally distinct components.

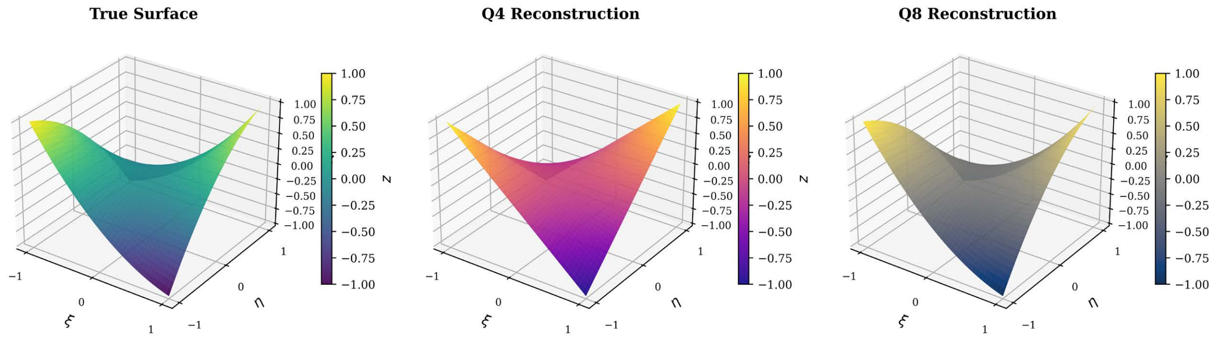

Figure 3. Saddle surface comparison. True saddle surface and Q4 and Q8 reconstructions. Q4 recovers the bilinear twisting component but fails to reproduce the quadratic curvature terms; Q8 reconstructs the full saddle to numerical precision.

The first is the bilinear term $\xi\eta$, which belongs to the Q4 polynomial span. The second is the quadratic terms ξ^2 and η^2, which do not. This mixture means Q4 is not completely blind to the saddle; it can detect and partially reproduce the twisting behavior, but it systematically misses the additional bending captured by the quadratic terms.

The Q4 reconstruction panel shows a surface with the correct general orientation and twisting character of a saddle, yet it visibly deviates from the true shape, particularly away from the element center. The resulting height RMSE is 0.1419 and the normal-angle error is 20.97 degrees. These errors are smaller than the dome case, consistent with the fact that Q4 at least captures the $\xi\eta$ component, but they remain substantial and would meaningfully distort any downstream geometric measurement.

The Q8 reconstruction again achieves machine-precision accuracy, with height RMSE of 6.78×10^{-17} and normal-angle error of 2.19×10^{-7} degrees. This confirms that Q8's polynomial span encompasses both the bilinear and the quadratic components of the saddle simultaneously. The saddle experiment is important because it demonstrates that partial polynomial overlap, Q4 capturing $\xi\eta$ but not ξ^2 or η^2, does not translate into acceptable geometric fidelity. An interpolant must contain the full polynomial content of the surface to reconstruct it accurately. The saddle belongs to $\mathcal{P}_{\text{Q8}} \setminus \mathcal{P}_{\text{Q4}}$. The Q4 height RMSE of 0.1419 is smaller than the dome case because Q4 captures the $\xi\eta$ bilinear component. Nevertheless, the normal-angle error of 20.97° indicates substantial geometric distortion from the missing quadratic terms. Q8 achieves machine-precision accuracy across all metrics, confirming Theorem 1 (ii).

6.3. Transcendental Ripple Results

Figure 4 shows the transcendental ripple reconstruction comparison panels. The ripple surface $z = 1/2\sin(2\xi)\cos(2\eta)$ is the most practically important of the three test cases because it lies outside the polynomial span of both Q4 and Q8. No finite serendipity polynomial can represent a transcendental function exactly, so this experiment measures approximation quality rather than exact reproduction.

This situation is representative of real-world surfaces encountered in depth imaging, structured-light scanning, and biomedical reconstruction, which are almost never exact low-order polynomials.

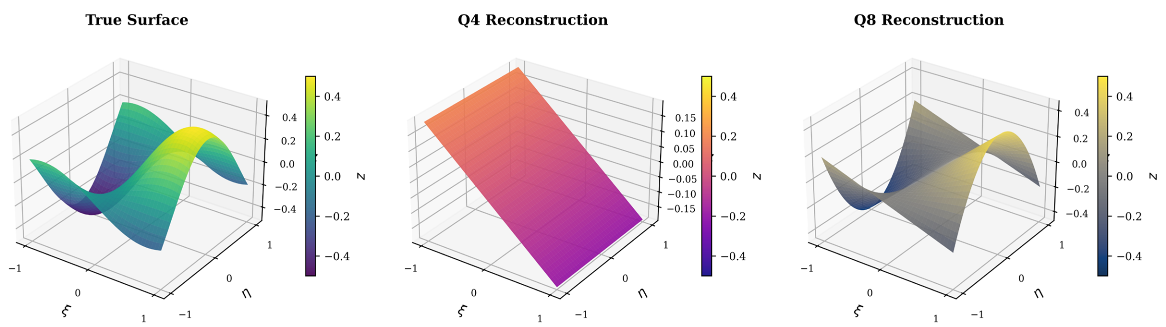

Figure 4. Transcendental ripple comparison. True transcendental ripple surface and Q4 and Q8 reconstructions. Neither method is exact, but Q8 substantially reduces height and shape error relative to Q4.

The Q4 reconstruction panel shows a severely smoothed and distorted version of the ripple. Q4's bilinear form cannot capture the oscillatory curvature of the ripple, producing a height RMSE of 0.3310 and a normal-angle error of 37.47 degrees—the largest normal error among all test cases. The surface orientation is almost entirely wrong over much of the element.

The Q8 reconstruction is not exact, as expected, but it is substantially better. The reconstructed surface follows the ripple's shape far more closely, reducing height RMSE to 0.0843 (a 74.5% reduction or a factor of approximately 3.93) and normal-angle error to 15.02 degrees. The maximum height error falls from 0.6576 to 0.1955. Visually, the Q8 panel captures the curvature undulation of the ripple in a way that Q4 does not. This result supports a balanced conclusion: Q8 does not solve the approximation problem for arbitrary smooth surfaces, but it provides a meaningfully better local geometric model. For applications where approximate but curvature-aware interpolation is sufficient, such as filling small missing-depth regions on smooth surfaces, Q8 offers a practical advantage over Q4 even when the surface is non-polynomial.

Since $z_{\text{ripple}} \notin \mathcal{P}_{\text{Q8}}$, both interpolants are approximate. Q8 reduces the height RMSE from 0.3310 to 0.0843, a factor of approximately 3.93. This ratio is consistent with the expected qualitative advantage of Q8 over Q4 but should be interpreted as a single-element approximation rather than a direct measure of the asymptotic convergence order. A separate mesh-refinement study with $h \to 0$ would be required to estimate convergence rates numerically. The normal-angle error decreases from 37.47˚ to 15.02˚, and the curvature MAE decreases from 1.8504 to 0.9856, corresponding to a 46.7% reduction.

6.4. Hessian Curvature Error Maps

Figure 5 shows the Hessian curvature magnitude error maps for all three surfaces. The Hessian curvature magnitude $\kappa_H = \sqrt{\left(z_{\xi\xi}\right)^2 + 2\left(z_{\xi\eta}\right)^2 + \left(z_{\eta\eta}\right)^2}$ measures the local bending strength of a surface at every point. Unlike the Laplacian, which can mask saddle-like curvature through cancellation of positive and negative components, the Hessian magnitude provides a reliable scalar indicator of how strongly the surface bends regardless of the sign of curvature.

The left column of each row in Figure 5 shows the true κ_H field. For the dome, κ_H is nearly uniform across the element, reflecting its constant quadratic bending. For the saddle, κ_H is spatially varying, with stronger bending near the edges due to the combined quadratic and bilinear structure. For the ripple, κ_H is highly spatially varying, reflecting the oscillatory nature of the true surface.

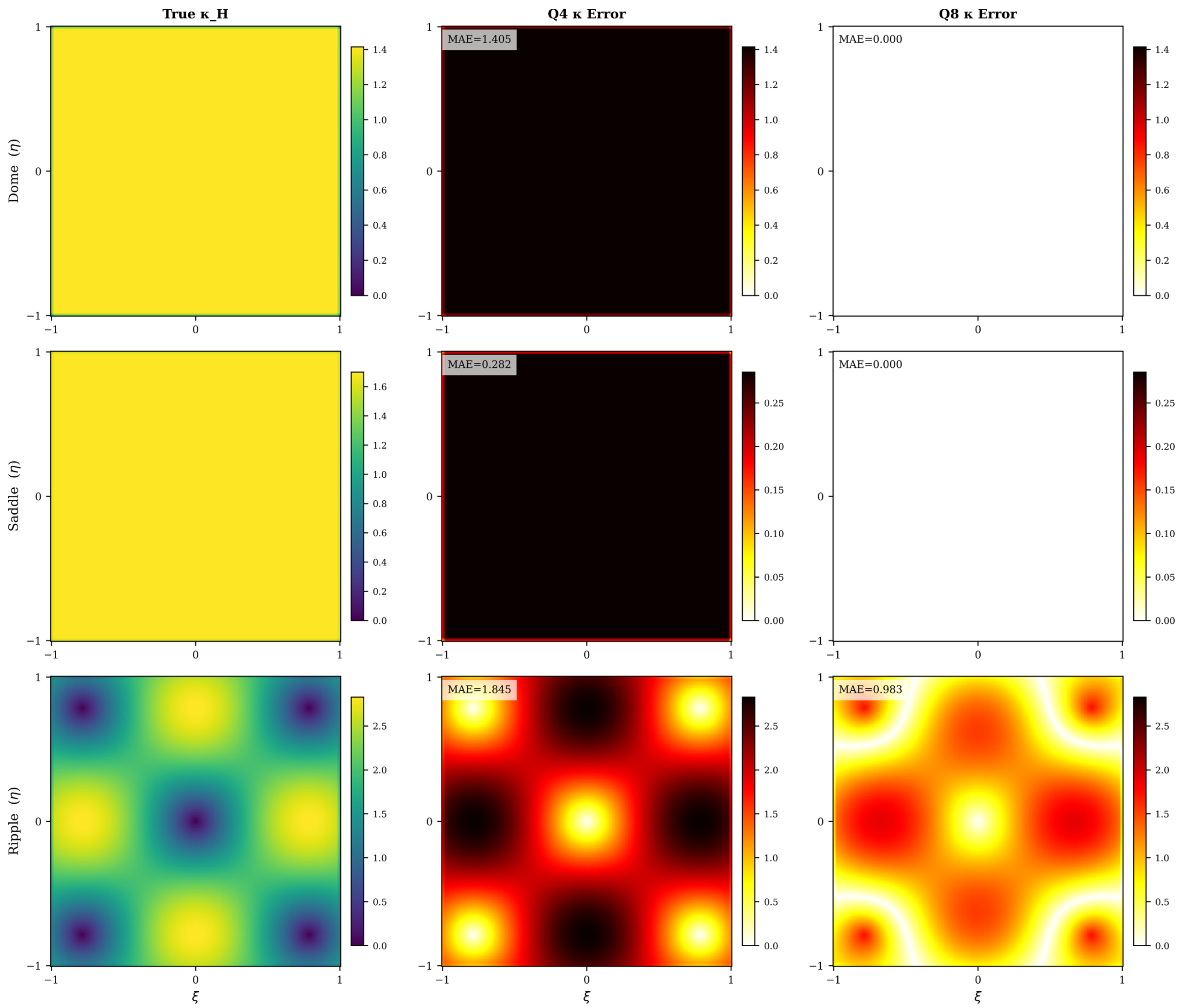

Figure 5. Hessian curvature magnitude error maps. Color maps of true Hessian curvature magnitude κ_H and absolute curvature error for Q4 and Q8 across all three test surfaces. Q4 errors are large and spatially structured; Q8 errors are near zero for the dome and saddle, and substantially reduced for the ripple.

The middle column shows Q4 curvature error. For the dome, Q4's error is large and spatially uniform—since Q4 produces a flat reconstruction, it contributes zero curvature everywhere and the error equals the true κ_H at every point, giving a curvature MAE of 1.4142. For the saddle, Q4 errors are concentrated in regions where the quadratic terms dominate over the bilinear term. For the ripple, Q4 curvature error is large and spatially structured, with a MAE of 1.8504, larger even than on the dome or saddle because the ripple's oscillatory curvature is entirely outside Q4's reach.

The right column shows Q8 curvature error. For the dome and saddle, Q8 error maps are visually indistinguishable from zero, the color scales register only machine-precision residuals (MAE on the order of 10^{-13}). For the ripple, Q8 error is visible but meaningfully smaller than Q4, with MAE falling from 1.8504 to 0.9856. The shared color scale used for the Q4 and Q8 error columns within each row ensures that the visual comparison is fair. This figure reinforces the key finding: Q8 preserves not only surface height but also the second-derivative structure that defines local shape.

6.5. Centerline Profiles

Figure 6 shows the centerline profiles. It shifts attention from surface height to second-derivative geometry. Figure 6 provides a one-dimensional cross-sectional view of the reconstruction quality, slicing each surface along the centerline $\eta = 0$. This representation complements the 3D surface plots and 2D error maps by showing the exact numerical profile of height and curvature along a single line, making it easy to see where and by how much each method deviates from the truth.

Dome (top row): The left panel shows the true dome profile along $\eta = 0$, which is the parabola $z = 1 - \xi^2/2$, with a peak of 1.0 at the origin and values of 0.5 at $\xi = \pm 1$. The Q4 profile is the horizontal line $z = 0$, because all four corner nodes of the full element have a value of zero. Along the centerline, this misses both the peak at $\xi = 0$ and the true centerline endpoint values $z = 0.5$ at $\xi = \pm 1$. The Q8 profile overlays the true curve exactly. The curvature panel shows the same pattern: Q8 matches the constant Hessian curvature proxy, while Q4 contributes zero curvature.

Saddle (middle row): Along $\eta = 0$, the true saddle reduces to $z = \xi^2/3$, so Q4 misses the parabolic centerline curvature entirely, while Q8 reproduces it exactly. The Q4 interpolant captures the bilinear component $\xi\eta$, which vanishes on this centerline, so the Q4 profile is the horizontal line $z = 0$, missing the parabolic profile. Q8 follows the true curve exactly, and the curvature panel confirms that Q8 preserves the nonzero ξ-direction centerline curvature ($\mathrm{d}^2 z/\mathrm{d}\xi^2 = 2/3$ along $\eta = 0$) while Q4 does not ($\mathrm{d}^2 z_{Q4}/\mathrm{d}\xi^2 = 0$ on this centerline, since $z_{Q4} = \xi\eta$ vanishes identically when $\eta = 0$). It is important to note, however, that the full 2D Hessian proxy for Q4 is nonzero because Q4 retains the mixed-derivative contribution from the $\xi\eta$ term. The curvature MAE of 0.285 in Table 3 reflects the difference between Q4 and the true Hessian-based curvature magnitude.

Ripple (bottom row): The ripple centerline $z = 1/2\sin(2\xi)$ is an oscillating curve that neither method reproduces exactly. However, the Q8 profile follows the oscillation much more closely than Q4, tracking the peaks and troughs with substantially smaller deviation. The curvature profile shows the same: Q8 captures the sign and approximate magnitude of the curvature variation, whereas Q4 produces a much flatter, less informative curvature estimate. The remaining discrepancy between Q8 and the true ripple is an honest representation of the approximation error inherent to any finite polynomial element on a transcendental surface.

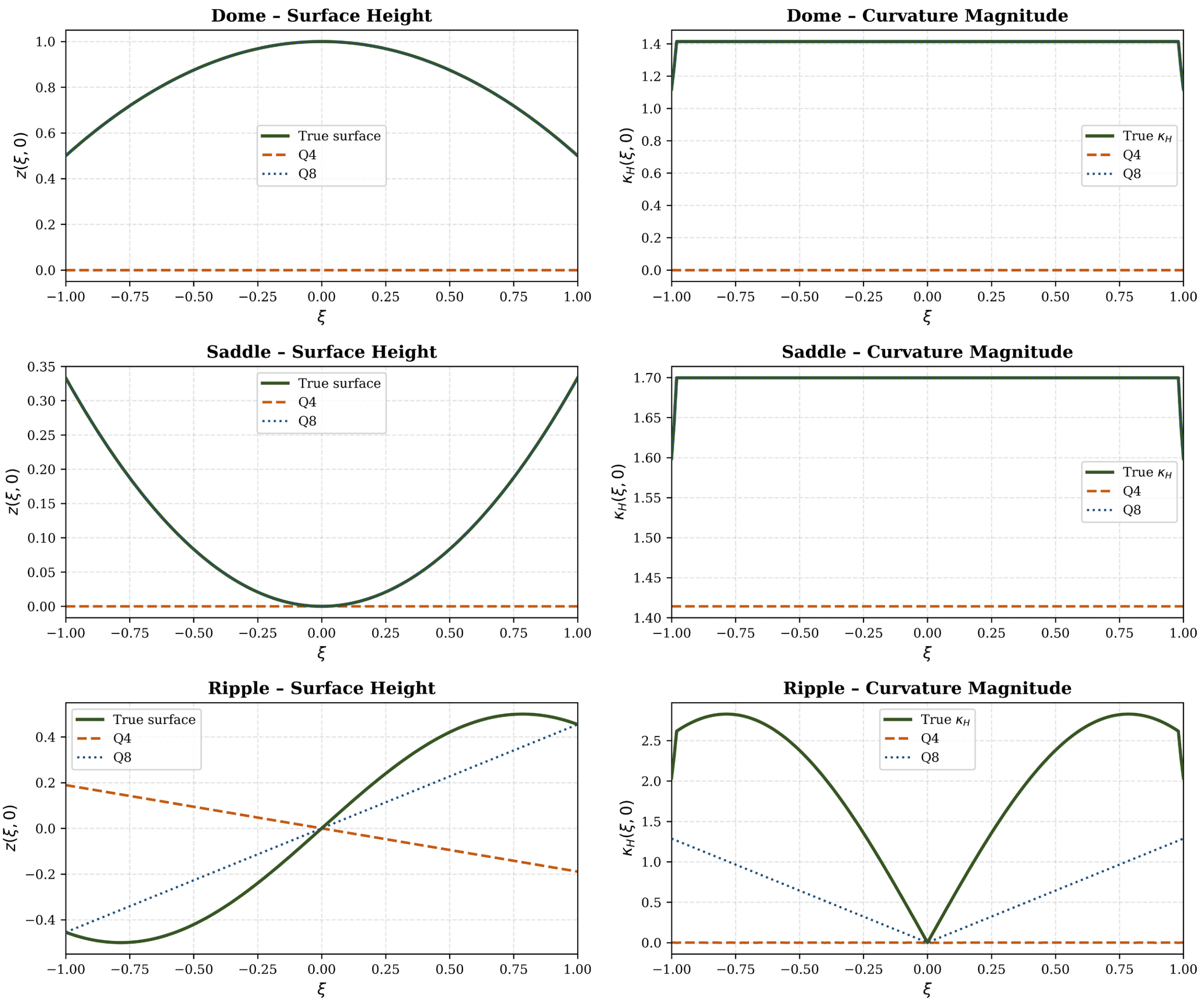

Figure 6. Centerline profiles. Surface height and Hessian curvature magnitude profiles along η = 0 for all three test surfaces, comparing the true surface against Q4 and Q8 reconstructions.

The ripple surface is the most application-relevant test because it lies outside both interpolation spaces. Neither Q4 nor Q8 can reconstruct it exactly. Nevertheless, Q8 substantially improves the approximation. The height RMSE decreases from 0.3310 for Q4 to 0.0843 for Q8, a reduction of approximately 74.5%. The maximum height error decreases from 0.6576 to 0.1955. The normal-angle error decreases from 37.47 degrees to 15.02 degrees. The curvature proxy error also decreases, although it remains nonzero. This is expected because the ripple contains transcendental variation that cannot be represented exactly by Q8. The observed error ratio of approximately 3.93 is consistent with the expected qualitative advantage of Q8 over Q4, but it should be interpreted as a single-element approximation result rather than a direct measurement of asymptotic convergence order. A separate mesh-refinement study with $h \to 0$ would be required to estimate convergence rates numerically.

7. Computational Trade-Off and Selection Criteria

This section translates the theoretical Sobolev-norm comparison and the single-element experiments into practical guidance, outlining the computational trade-offs between Q4 and Q8 and specifying when each interpolant is the more appropriate choice for curvature-sensitive surface reconstruction.

7.1. Arithmetic and Sampling Cost

Q4 evaluates 4 shape functions; Q8 evaluates 8. Both remain $O(1)$ per interpolation point and require no iteration, global system assembly, or training. The more consequential cost is the requirement of reliable edge-midpoint nodal values for Q8. If these are unavailable or noisier than corner samples, the Q8 approximation advantage may be compromised.

7.2. Theory-Grounded Selection Criteria

The criterion below is valid under three conditions. First, the surface must be sufficiently smooth: $f \in H^2(\Omega)$ for the Q4 bounds and $f \in H^3(\Omega)$ for the Q8 bounds, so that the Sobolev seminorms in Theorem 2 are finite. Second, the element mapping must be affine (or at least regularly bounded), so that the Bramble–Hilbert constants scale independently of h. Third, the Q8 midpoint nodal values must be reliable; as noted in **Table 4**, high noise at midpoint nodes undermines the approximation advantage that motivates the Q8 choice. When any of these conditions are violated, the table below should be applied with caution.

The theoretical comparison in **Table 2** shows that Q8 achieves one higher order of convergence than Q4 at every Sobolev norm level: L^2 (heights), H^1 (slopes and normals), and H^2 (curvature). Together with the Monge-patch curvature analysis in Section 3, this yields a clear set of selection criteria for sparse surface reconstruction:

- **Height-only accuracy (L^2).** Q4 achieves $\mathcal{O}(h^2)$ convergence in L^2, whereas Q8 achieves $\mathcal{O}(h^3)$. When the application uses only height information on locally planar or bilinear patches, the extra order of Q8 may not justify its additional nodal and computational cost, and Q4 is typically sufficient.
- **Normal and slope accuracy (H^1).** Surface normals depend on first derivatives of the height field, so normal errors are governed by the H^1 interpolation error. Q4 yields $O(h)$ convergence in H^1, whereas Q8 yields $\mathcal{O}(h^2)$. For tasks that use normals downstream—such as shading, registration, nor-

mal-based matching, or biomechanical analysis—Q8 is theoretically preferred, because it provides faster decay of orientation error under mesh refinement.

- **Curvature and shape accuracy (H^2).** The Hessian-based curvature proxy κ_H is equivalent to the H^2 seminorm of the Monge-patch height field, so curvature errors are governed by the H^2 interpolation error. In this norm, Q4 has only an $\mathcal{O}(h^0)$ bound, meaning the theoretical curvature-level error does not decrease with refinement, while Q8 attains $O(h)$. For curvature-sensitive reconstruction, or whenever bending and local shape carry physical meaning, Q8 is the better-suited interpolant within the Q4 - Q8 family [7] [13] [14].

In practical terms, Q4 is appropriate for height-only interpolation on locally planar or bilinear elements, especially when only corner samples are available or computational cost is dominant. Q8 is justified when reliable edge-midpoint samples are available and higher-order control of surface normals or curvature is required, as in the dome, saddle, and ripple examples in Section 6.

7.3. Practical Selection Table

Table 4 aggregates the theoretical and numerical findings into practical guidance for choosing between Q4 and Q8 in sparse surface reconstruction. Rather than presenting Q8 as universally superior, the table highlights the specific conditions under which each interpolant is mathematically and computationally appropriate. Rows associated with height accuracy reflect the L^2 orders from Theorem 2; rows involving normals and edge geometry reflect the H^1 behavior; and rows involving curvature or the Hessian-based proxy κ_H reflect the H^2 behavior. This makes the engineering recommendations traceable directly back to the Sobolev-norm comparison in **Table 2** and the curvature analysis in Section 3.

Table 4. Practical selection criteria for Q4 and Q8 interpolation.

Reconstruction Condition	Prefer Q4	Prefer Q8
Surface is locally planar	Yes	Not needed
Surface is locally bilinear	Yes	Not needed
Pure curvature required (H^2 accuracy)	No	Yes (positive-order H^2 convergence)
Edge curvature matters	No	Yes
Normals used downstream (H^1 accuracy)	Sometimes acceptable	Preferred
Only corner samples available	Yes	No
Midpoint samples available	Optional	Yes
Computational simplicity dominant	Yes	Sometimes
Smooth anatomical or depth surface	May be	Yes
Sharp discontinuities dominate	Neither	Edge-aware method
Nodal noise is high	Possibly	Use regularization

The first two rows address locally planar and bilinear surfaces. In these cases, Q4 is sufficient, and Q8 is unnecessary. Q4's polynomial span exactly contains flat and bilinear fields, so adding midpoint nodes provides no additional accuracy while increasing sampling cost. In nearly planar regions, common in man-made environments, flat tissue surfaces, or background depth maps, Q4 is the pragmatic choice.

Rows three and four address curvature and edge shape. When pure bending or parabolic edge profiles are present, Q8 is clearly preferred. These rows capture the core finding of the paper: Q8's inclusion of ξ^2 and η^2 in its polynomial span is the critical structural advantage over Q4 for curved-surface reconstruction.

Rows five through seven address downstream usage and data availability. If surface normals are used downstream—for rendering, registration, shape matching, or biomechanical analysis—Q8 is preferred because it produces more accurate normals. If only corner samples are available, Q8 cannot be used without midpoint estimation; Q4 is then the appropriate choice. If midpoint samples are available, Q8 should be considered.

Row eight addresses computational simplicity. In real-time systems, embedded implementations, or very large-scale reconstructions where per-element cost matters, Q4's lower arithmetic count may be decisive. Q8's extra shape functions are modest in absolute terms, but in computationally constrained settings, Q4 may still be preferred.

Rows nine through eleven handle special cases. Smooth anatomical or depth surfaces—the primary application targets—favor Q8 when curvature matters. Sharp discontinuities, such as object boundaries, anatomical folds, or depth edges, should not be handled by either Q4 or Q8 alone; edge-aware segmentation or boundary-detection pre-processing is needed before any element-based interpolation. High nodal noise warrants caution: while Q8 provides better curvature fidelity with clean data, using more samples can amplify noise if the midpoint measurements are unreliable, and regularized or filtered variants may be needed.

8. Application Relevance

The theoretical and computational findings are relevant to several sparse surface reconstruction problems. In depth-map completion, the H^1 convergence advantage of Q8 predicts better normal accuracy in smooth regions, making it a principled, lightweight geometry-preserving operator [3] [4]. In structured-light scanning, Q8 can reconstruct missing curved patches with second-order H^1 accuracy, preserving the parabolic edge geometry that Q4 would chord away. In biomedical surface reconstruction, under the smoothness and exact-nodal-data assumptions of the interpolation estimate, Q8 predicts first-order convergence of Hessian-based curvature quantities, which is relevant to volume estimation, registration, and biomechanical modeling [5]. In endoscopic reconstruction, Q8's H^1 accuracy supports normal-based matching in structure-from-motion and stereo pipelines. In sparse landmark deformation modeling, Q8 provides one higher order of convergence in the deformation gradient than Q4, which matters for strain estimation and soft-tissue biomechanics.

It should be noted that the applications above use assembled multi-element meshes rather than a single isolated reference element; the interpolation properties established in this paper apply locally to each element patch, and questions of inter-element continuity, global consistency, and mesh-assembly effects are outside the present scope and are left to future multi-element studies. Across these applications, Q8 should be viewed as a local reconstruction primitive whose theoretical grounding is in polynomial completeness and Sobolev approximation theory, and whose practical justification holds when the surface is smooth, curved, and sufficiently sampled.

9. Limitations and Future Work

The Bramble-Hilbert bounds of Theorem 2 apply under the assumption $f \in H^{p+1}(\Omega)$. If f contains discontinuities, the Sobolev seminorm $|f|_{H^{p+1}}$ is unbounded, and the bounds do not apply [13]-[15]. Q8 should therefore not be applied across surface discontinuities, depth edges, anatomical folds, object boundaries, or surgical instrument contacts, without edge-aware pre-processing. When an element straddles a discontinuity, Q8 may produce a smooth but physically incorrect surface.

The interpolation error bounds also assume exact nodal data. When midpoint values carry measurement noise δ, Q8 inherits an additional error proportional to $\max_k |\delta_k| \|\phi_k\|_{L^\infty(\Omega)}$, which does not decrease with h. Regularized Q8 formulations should be investigated for noisy settings, and future work should quantify the noise amplification factor for Q8 relative to Q4 under controlled additive noise models.

A natural extension is adaptive Q4/Q8 selection driven by local curvature indicators: if a curvature estimator exceeds a threshold, Q8 is applied; otherwise, Q4 suffices. Future studies should evaluate both elements on real datasets, including public depth maps, structured-light scans, organ segmentation surfaces, and endoscopic data, and should develop anisotropic error estimates for stretched elements and convergence analysis under isoparametric mappings.

10. Conclusion

This paper provided a mathematically rigorous comparison of Q4 and Q8 interpolation for curvature-sensitive sparse surface reconstruction. The theoretical layer established polynomial completeness degrees ($p=1$ for Q4, $p=2$ for Q8), proved exact polynomial reproduction (Theorem 1), derived Bramble-Hilbert interpolation error bounds predicting one higher order of Sobolev convergence for Q8 at every level L^2, H^1, H^2 (Theorem 2), and grounded the curvature and normal metrics in Monge patch differential geometry. The computational layer confirmed the polynomial reproduction predictions: Q8 achieved machine-precision errors on the quadric dome and saddle surfaces, while Q4 produced substantial errors in the height, curvature proxy, and normal angle due to its missing pure quadratic terms. For the transcendental ripple, which lies outside both interpolation spaces, Q8 reduced height RMSE by 74.5%, reduced normal-angle error from 37.47˚ to 15.02˚, and reduced curvature-proxy MAE from 1.8504 to 0.9856, corresponding to a 46.7% reduction. These results support the selection criterion derived from the Sobolev hierarchy: Q8 is better suited for curvature-sensitive applications requiring positive-order H^2-level behavior, while Q4 remains appropriate for height-only applications on locally planar or bilinear surfaces. All reported error values arise from single-element tests on analytically defined surfaces over the fixed master element. They demonstrate polynomial reproduction and single-element approximation behavior, but they do not measure asymptotic convergence order.

Conflicts of Interest

The author declares no conflicts of interest regarding the publication of this paper.

References

[1] Zienkiewicz, O.C., Taylor, R.L. and Zhu, J.Z. (2013) The Finite Element Method: Its Basis and Fundamentals. 7th Edition, Butterworth-Heinemann.

[2] Hughes, T.J.R. (2000) The Finite Element Method: Linear Static and Dynamic Finite Element Analysis. Dover Publications.

[3] Khan, M.A.U., Nazir, D., Pagani, A., Mokayed, H., Liwicki, M., Stricker, D., *et al.* (2022) A Comprehensive Survey of Depth Completion Approaches. *Sensors*, **22**, Article 6969. https://doi.org/10.3390/s22186969

[4] Zhang, Y. and Funkhouser, T. (2018) Deep Depth Completion of a Single RGB-D Image. 2018 *IEEE/CVF Conference on Computer Vision and Pattern Recognition*, Salt Lake City, 18-23 June 2018, 175-185. https://doi.org/10.1109/cvpr.2018.00026

[5] Antonelli, M., Reinke, A., Bakas, S., *et al.* (2022) The Medical Segmentation Decathlon. *Nature Communications*, **13**, Article No. 4128.

[6] Strang, G. and Fix, G.J. (2008) An Analysis of the Finite Element Method. 2nd Edition, Wellesley-Cambridge Press.

[7] Brenner, S.C. and Scott, L.R. (2008) The Mathematical Theory of Finite Element Methods. 3rd Edition, Springer. https://doi.org/10.1007/978-0-387-75934-0

[8] Ciarlet, P.G. (2002) The Finite Element Method for Elliptic Problems. Society for Industrial and Applied Mathematics. https://doi.org/10.1137/1.9780898719208

[9] Arnold, D., Boffi, D. and Falk, R. (2002) Approximation by Quadrilateral Finite Elements. *Mathematics of Computation*, **71**, 909-922. https://doi.org/10.1090/s0025-5718-02-01439-4

[10] Kikuchi, F., Okabe, M. and Fujio, H. (1999) Modification of the 8-Node Serendipity Element. *Computer Methods in Applied Mechanics and Engineering*, **179**, 91-109. https://doi.org/10.1016/s0045-7825(99)00031-6

[11] Ern, A. and Guermond, J.L. (2004) Theory and Practice of Finite Elements. Springer. https://doi.org/10.1007/978-1-4757-4355-5

[12] Patrikalakis, N.M., Maekawa, T. and Cho, W. (2009) Shape Interrogation for Computer Aided Design and Manufacturing.

https://web.mit.edu/hyperbook/Patrikalakis-Maekawa-Cho/

[13] Bramble, J.H. and Hilbert, S.R. (1970) Estimation of Linear Functionals on Sobolev Spaces with Application to Fourier Transforms and Spline Interpolation. *SIAM Journal on Numerical Analysis*, **7**, 112-124. https://doi.org/10.1137/0707006

[14] Bramble, J.H. and Hilbert, S.R. (1971) Bounds for a Class of Linear Functionals with Applications to Hermite Interpolation. *Numerische Mathematik*, **16**, 362-369. https://doi.org/10.1007/bf02165007

[15] Adams, R.A. and Fournier, J.J.F. (2003) Sobolev Spaces. 2nd Edition, Elsevier.